Comparative study of hydrotalcite-derived supported Pd2Ga and PdZn intermetallic nanoparticles as methanol synthesis and methanol steam reforming catalysts

Synthesis, Characterization and Comparative Catalytic Study in Methanol Synthesis and Methanol Steam Reforming of Supported Pd_2Ga and PdZn Intermetallic Nanoparticles

Edward L. Kunkes [1], Antje Ota [1], Igor Kasatkin [1], Elena Groppo [2], Davide Ferri [3], Rufino M. Navarro Yerga [4], Malte Behrens [1,*]

[1] Fritz-Haber-Institute of the Max-Planck-Society, Department of Inorganic Chemistry, Faradayweg 4-6, D-14195 Berlin, Germany

[2] University of Torino, Department of Inorganic, Physical and Material Chemistry, NIS Centre of Excellence and INSTM, Via P. Giuria 7, I-10125 Torino, Italy

[3] Empa, Swiss Federal Laboratories for Materials Science and Technology, Laboratory for Solid State Chemistry and Catalysis, Ueberlandstrasse 129, CH–8600 Dübendorf, Switzerland

[4] Instituto de Catálisis y Petroleoquímica (ICP), Departamento de estructura y reactividad de catalizadores (EAC), Madrid, Spain

* behrens@fhi-berlin.mpg.de, Tel: +49 30 8413-4408, Fax: +49 30 8413-4405

Abstract

Supported PdZn, Pd_2Ga and Pd catalyst were synthesized by reductive decomposition of ternary Hydrotalcite-like compounds. The precursors and resulting catalysts were characterized by HRTEM, XRD, XAS and CO-IR spectroscopy. The Pd^{2+} cations were found to be at least partially incorporated into the cationic slabs of the precursor. Full incorporation was confirmed for the PdZnAl-Hydrotalcite-like precursor. After reduction of Ga- and Zn-containing precursors the intermetallic compounds Pd_2Ga and PdZn were present in form of nanoparticles with an average diameter of 6 nm or less. Tests of catalytic performance in methanol steam reforming and methanol synthesis from CO_2 have shown that the presence of Zn and Ga improves the selectivity to CO_2 and methanol respectively. The catalysts containing intermetallic compounds were 100 and 200 times respectively more active for methanol synthesis than the monometallic Pd catalyst. The beneficial effect of Ga in the active phase was found to be more pronounced in methanol synthesis compared to steam reforming of methanol, which probably is related to insufficient stability of the reduced Ga species in the more oxidizing feed of the latter reaction. Although the intermetallic catalysts were, in general less active than a Cu/ZnO-based material prepared by a similar procedure, the marked changes in Pd reactivity upon formation of intermetallic compounds render our precursor-method a versatile approach for studying the tunability of Pd-based catalysts for different reactions.

1. Introduction

Methanol has been proposed as a promising energy storage molecule for portable applications such as direct methanol fuel-cells, as well as fuel for automobile internal combustion engines [1]. Additionally methanol has been proposed as hydrogen storage medium [2-4], whose gravimetric hydrogen density exceeds that of compressed and even that of liquid hydrogen. Furthermore, the use of CO_2 as a carbon source for methanol synthesis enables the simultaneous reduction of emissions of this proven greenhouse gas [1].

Methanol synthesis from CO_2 (Reaction 1) and its reverse reaction, methanol steam reforming (MSR) comprise a class of reactions critical to the application of methanol as an efficient energy carrier.

$$CO_2 + 3H_2 \leftrightarrows CH_3OH + H_2O \quad \Delta H_0 = -49.8 \frac{kJ}{mol} \qquad (1)$$

$$CO_2 + H_2 \leftrightarrows CO + H_2O \quad \Delta H_0 = +41.2 \frac{kJ}{mol} \qquad (2)$$

$$CH_3OH \leftrightarrow CO + 2H_2 \quad \Delta H_0 = +91.0 \frac{kJ}{mol} \qquad (3)$$

Both reactions are currently carried out at similar temperatures (250-330 °C) on Cu/ZnO based catalysts. While MSR is not thermodynamically limited and is carried out at atmospheric pressure, methanol synthesis requires high pressures (30-100 bar) and lower operating temperatures due to unfavorable thermodynamics.[5] Reverse water gas shift (rWGS, Reaction 2) is a side reaction to methanol synthesis and thus diminishes selectivity. In MSR, methanol decomposition (Reaction 3) as well as rWGS are undesired side reactions and yield CO- a poison for fuel cell electrodes. The rates of both undesired reactions can be thermodynamically hindered by operating at lower temperatures. Lower temperature operation and low selectivity to rWGS or decomposition thus remain the driving forces behind the development and optimization of methanol catalysts.[5]

The current state of the industrial Cu/ZnO catalysts are well suited to stationary operation, however suffer from pyrophoricity, sintering with long reaction times and instability to changes in reaction conditions.[6] These shortcomings make Cu-based catalysts unsuitable for portable applications. To that end, Pd supported on reducible oxides such as ZnO, In_2O_3 and Ga_2O_3 has shown favorable reactivity similar to that of Cu-based catalysts for both methanol synthesis and MSR [7, 8], whereas Pd supported on inert supports has been shown to be selective to rWGS and methanol decomposition. Additionally, Pd based catalysts have also

shown good long-term stability and resistance to sintering. The alteration of the properties of Pd was attributed to the formation of the intermetallic compounds (IMCs) Pd_2Ga [9-11] and PdZn [7, 12-14] upon partial reduction of the support components. An intimate interaction between Pd and these support components is therefore thought to be prerequisite to the formation of IMCs.

In that respect, we recently developed a facile wet chemical synthesis approach to prepare Pd-Ga intermetallic nanoparticles. Pd_2Ga nanoparticles supported on oxide matrix of MgO and $MgGa_2O_4$ were synthesized by co-precipitation of a single phase precursor, followed by thermal decomposition.[15] This method presents an efficient alternative to the previously used top- down approaches, such as etching or milling of materials obtained from high temperature melt synthesis .[16] Ternary hydroxycarbonates, so called Hydrotalcite-like compounds (HTlc), were used as precursors. The advantage of these materials is that M^{II} and M^{III} cations are uniformly distributed in slabs of edge-sharing MO_6 octahedra that allow a close interaction of all metal cations.[17, 18] HTlc exhibit the general composition $(M1^{II},M2^{II})_{1-x}M3^{III}_x(OH)_2(CO_3)_{x/2}\cdot$ m H_2O ($0.25 \leq x \leq 0.33$) and a huge flexibility of metal cations that can be incorporated into the structure, such as M^{II} = Mg^{2+}, Mn^{2+}, Co^{2+}, Ni^{2+}, Cu^{2+}, Zn^{2+} and M^{III} = Al^{3+}, Ga^{3+}, Fe^{3+}, Cr^{3+}.[19] In our previous work [15] HTl having M^{II} = Mg^{2+} and Pd^{2+} and M^{III} = Ga^{3+} were used to form the precursor of the Pd_2Ga phase. Herein, we will present a systematic comparative study of metal-oxide supported Pd and intermetallic Pd-X (X = Ga, Zn) nanoparticles derived from ternary Pd based Hydrotalcite-like compounds. PdMgGa, PdZnAl and PdMgAl-HTlc´s were synthesized by co-precipitation and undergo the formation of well-dispersed Pd-Ga, Pd-Zn and Pd nanoparticles (2-6 nm) respectively during reduction.

As all catalysts were derived from a similar well-defined precursor material, aspects of different preparation history, inhomogeneous microstructures, and variations in metal-support contacts, that often complicate the comparison of catalyst, should only play a minor role here. Thus, the aim of this study is to use these materials to investigate the role of different Pd-based IMCs in different reactions involving methanol, namely its synthesis from CO_2 and the reverse MSR. In addition to the catalytic performance data, we report on catalyst synthesis and present characterization data using a variety of complementary techniques (XRD, BET, TPR, SEM, TEM, FTIR, XANES) to correlate structural properties with activity.

2. Experimental

2.1. Synthesis conditions

Ternary palladium containing and binary Pd-free PdMgAl, PdMgGa, PdZnAl, MgGa, ZnAl and MgAl HTlc's with M^{2+}:M^{3+} molar ratios of 70:30 were synthesized by co-precipitation. The nominal composition of all Pd-M^{2+}-M^{3+} samples was set to 1:69:30. A mixed aqueous metal nitrate ([Pd^{2+}] + [M^{2+}] + [M^{3+}] = 0.2 M) and 0.345 M basic solution as precipitating agent were co-feed at pH = 8.5. For MgGa and MgAl HTlc precursors pure sodium carbonate solution and a precipitation temperature of 55 °C were used, whereas in case of PdZnAl HTlc a mixture of sodium carbonate (0.3 M) and sodium hydroxide (0.045 M) and a temperature of 25 °C have be applied in order to obtain an homogeneous precursor sample. During precipitation both solutions were added simultaneously dropwise into a 2 L precipitation reactor (Mettler-Toledo LabMax). The nitrate solution was automatically pumped with a constant dosing rate and the basic solution was added to maintain a constant pH of 8.5. After completion of addition, the mixture was aged for 1 h at the same temperatures applied during synthesis. The precipitate was filtered and washed twice with warm deionized water in order to remove the nitrate and sodium ions and obtain a conductivity of the filtrate lower than 0.2 mS/cm. The solid was dried for 12 hours at 80 °C in air. After drying a one-step decomposition-reduction in 5% H_2 in Ar was performed at 250/500 °C (2°/min) that yielded in the intermetallic phases and in metallic Pd in case of the PdMgAl HTlc precursor. A reduction temperature of 250 °C was applied for the PdMgAl and PdZnAl system, whereas a reduction of 500 °C is needed to obtain Pd_2Ga intermetallic particles.

As reference material for the catalytic test in methanol synthesis a HT-based CuZnAl catalyst was prepared as described previously.[20] Additional information about the synthesis conditions of the CuZnAl HTlc precursor and the synthesis protocols of the Pd-based HTlc's are given in the supplementary (S 1).

2.2. Characterization

X-ray diffraction. XRD patterns of the HTlc precursor and its decomposition products were recorded on a STOE Stadi P diffractometer in transmission geometry using Cu $K\alpha_1$ radiation, a primary Ge monochromater and a 3° linear position sensitive detector.

Specific surface area determination. Specific surface areas (SSA) of the precursors and reduced compounds were determined by N_2 adsorption–desorption measurements at 77K by employing the BET method (Autosorb-1C, Quantachrome). Prior to N_2 adsorption, the sample was outgassed at 80°/150 °C (precursor sample / reduced catalyst, respectively) to desorb moisture from the surface and pores.

Chemical Analysis. About 5 mg were exactly weighted in and dissolved in 2 ml aqua regia. The solutions were transferred and filled up in 50 ml volumetric flasks. The content of the metals were determined with ICP-OES (Vista RL, Varian) after matrix matched calibration.

Temperature programmed reduction. The TPR experiments were performed in a fixed bed reactor using 400 mg of precursor (100-250 µm sieve fraction). Precursors were reduced in 5 vol% H_2 in Argon (100 ml/min) up to a sample temperature of 500 °C (2°/min). The temperature was kept constant for 4 hours. The hydrogen consumption was monitored with a thermal conductivity detector.

X-ray absorption near edge structure. XANES measurements at the Pd K edge (24.350 keV) were carried out at the Super-XAS beamline at the Swiss Light Source (Villigen, Switzerland) in transmission, using ionization chambers as detectors and a Si(311) Quick EXAFS monochromator. A Pd foil placed between the second and third ionization chamber was measured simultaneously as an internal reference. In situ XANES measurements during hydrogen TPR were performed in transmission mode, using a capillary reactor cell. The precursor (63-100 µm, 30 mg) was filled in the capillary between quartz wool plugs. The cell was connected to a gas manifold. The cell was convectively heated by means of an air blower. Spectra were collected during the reduction in 5 Vol % H_2/N_2 (100 ml/min) in the temperature range of 30-500 °C. Data reduction was performed using the Athena 0.8.056 software package.

Fourier-Transformed infrared absorption spectroscopy. In situ experiments were carried out in a custom built quartz cell equipped with KBr windows allowing sample activation and successive measurements in the 25 – 550 °C temperature range, at pressures from 10^{-4} to 760 Torr. The catalysts were pressed into self-supporting pellets and activated in the same cell used for the measurement. The thermal treatments were performed either in dynamic vacuum or under static conditions (no flux), according to procedures discussed below. In situ FTIR spectra on the investigated catalysts were recorded at a resolution of 2 cm^{-1} on a Nicolet 6700 instrument, in transmission mode. Pd-Zn-Al and Pd-Mg-Al HTlc precursors were outgassed in dynamic vacuum up to 250 °C for several hours (until the pressure reached values below 10^{-4} Torr), followed by reduction in H_2 gas (2 cycles of 30 minutes, p_{H2} = 100 Torr). H_2 was removed from the cell at the same temperature and the sample was allowed to reach room temperature in dynamic vacuum. Pd-Ga-Mg HTlc precursor was outgassed in dynamic vacuum up to 550 °C for several hours (until the pressure reached values below 10^{-4} mbar), followed by reduction in H_2 gas (4 cycles of 1 h, P_{H2} = 100 Torr). H_2 was removed from the

cell at the same temperature and the sample was allowed to reach room temperature in dynamic vacuum.

Scanning electron microscopy. SEM images were acquired with a Hitachi S4800 FEG microscope equipped with an EDS system (EDAX) for elemental analysis. The samples were loosely dispersed on a conductive carbon tape to preserve the as-prepared morphology as much as possible. SEM images were acquired at low accelerating voltage, i.e. 1.5 kV, while EDX spectra were acquired at an accelerating voltage of 15 kV.

Electron Microscopy. HRTEM images were acquired using a FEI TITAN microscope, equipped with a field emission gun (FEG) and operated at 300 kV. With computer assisted correction and alignment, the value of the spherical aberration constant C_s was kept below 100 nm in the present experiments. Selected areas of the high resolution images have been Fourier transformed to obtain Power spectra and the lattice distances and angles were measured for phase identification (accuracy ± 1 % and ± 0.5°, respectively). Metal dispersions for Pd based catalysts were obtained by D = 1.1/d, where d is the average particle size determined by TEM. An estimate of the number of surface metal sites was calculated from this dispersion and the palladium loading. For bimetallic nanoparticles, incorporation of second metal (Zn or Ga) was assumed stoichiometric according to PdZn and Pd_2Ga.

2.3. Catalytic performance

2.3.1. Methanol synthesis from CO_2

Methanol synthesis experiments were carried out in a stainless steel fixed-bed flow reactor. 400 mg (100-200 μm) of HTlc precursor was mixed with 2 g of crushed SiO_2 chips and loaded into a 10 mm I.D. stainless steel reactor tube. Gas flows were controlled and monitored with analog mass flow controllers (Brooks 5850A).

The PdZnAl and PdMgAl HTlc precursors were reduced in situ at 250 °C (2°/min) for 2 hours in 100 ml/min (STP) of 20% H_2 in He. The PdMgGa HTlc precursor was reduced at 500 °C (2°/min) for 5 hours in the same H_2/He mixture. Upon completion of the reduction, the reactor was cooled to 250 °C, a 3:1 H_2/CO_2 mixture (100 ml/min) containing 4% Ar (as internal standard) was introduced into the reactor, and the pressure was raised to 30 bar by means of a back-pressure regulator (Tescom). The back pressure regulator and all high-pressure line were heated to 150 °C to avoid condensation of water and methanol, and all low-pressure lines downstream of the back-pressure regulator were heated to 120 °C. Online analysis of products was performed with a GC (Agilent 6890) equipped with a J&W

scientific Haysep Q Column and a TCD for analysis of non-condensable gases and a Agilent DB1 column interfaced to an FID for analysis of methanol. Methanol and CO were the main products observed, along with traces (less than 0.1% selectivity) of methane. After the start of the reaction, the catalysts were allowed to stabilize for 20 h time-on-stream at 250 °C. After this period, the activation energies of methanol synthesis and rWGS were measured in the temperature range of 190 – 275 °C, with 4 h allowed for each temperature point. Conversions of CO_2 were below 3% insuring the absence of thermodynamic artifacts.

2.3.2. Methanol steam reforming

Steam reforming of methanol (SRM) reaction was conducted using a fixed-bed flow reactor at 250 °C and atmospheric pressure. Activity tests were performed using 0.125 g of HTlc precursor diluted with SiC at volume ratio of 3:1 to avoid adverse thermal effects. Catalyst bed was placed in a 6 mm I.D. quartz tubular reactor with a coaxially centred thermocouple. Prior to reaction, the PdZnAl and PdMgAl HTlc precursors were reduced in situ at 250 °C (2°/min) for 4 hours in 60 cm³ (STP) of 5% H_2 in N_2. The PdMgGa HTlc precursor was reduced at 550 °C (2°/min) for 4 hours in the same H_2/N_2 mixture. The pretreating gases were flushed from the reactor with N_2 before admission of methanol-water-nitrogen reaction mixtures. Methanol and water mixture was supplied into a preheater by means of a liquid pump (Becton-Dickinson) before their mixture with nitrogen carrier supplied by Brooks model 5850E mass flow controller. For SRM reaction, the reactants were introduced into the reactor in the molar ratio H_2O/CH_3OH = 1.0. In the SRM tests, the total flow rate was kept at 26 ml/min (STP) and the methanol concentration in the feed gas mixture was fixed at 28.4 % (vol.) to avoid thermal effects derived from the high endothermicity of the reaction.

The reaction products were analyzed on-line by GC with TCD (HP 6890 GC) equipped with CP-Porabond Q (CO_2, water, methanol, formaldehyde, methyl formate and dimethyl ether) and molecular 5A (H_2, O_2, N_2, CO) connected in series, using He as carrier gas. Each value of total conversion is the average of two different analyses taken after 3h time-on-stream at a given temperature.

The hydrogen selectivity of the reaction was determined by comparing the molar hydrogen production rate to the maximum stoichiometrically allowable hydrogen production rate at a given methanol conversion (4).

$$S = \frac{r_{H_2}}{(3r_{MeOH})(4)}$$

If the reaction is dominated by SRM, H_2 and CO_2 selectivities should lie at around 100%, whereas if methanol decomposition is the primary reaction, the H_2 selectivity lies at 67% and the CO_2 selectivity near zero.

3. Results and discussion

3.1 Properties of the HTlc precursors

The XRD pattern of all as-synthesized precursor samples (Figure 1A, C and E) are typical of hydrotalcite-like structures. No other crystalline phases could be observed by XRD. The crystallinity of the precursors decreased in the order of PdMgGa > PdZnAl > PdMgAl as indicated by the increased peak broadening. In Table 1 the nominal composition of Pd containing and Pd-free HTlc precursors are listed. There are small deviations between the nominal and measured composition. In particular, the M^{3+} content of PdMgAl and PdMgGa HTlc is increased to 35 mol% and the Pd content of PdMgAl HTlc is slightly higher than 1 mol% (1.3 mol%).

The specific surface areas of the HTlc precursors, as obtained by nitrogen physisorption, varied between 34 and 127 m²/g (Table 1). The substitution of M^{2+} by Pd^{2+} result for all samples in an increase of the surface area, probably due to hindered growth of the Pd distorted HTlc lattice. In general, the surface area increases from PdMgGa < PdZnAl < PdMgAl, which is in agreement with the smaller crystallite size observed in the broader XRD line profiles. Differences in surface area and crystallite size are compatible with the observation of SEM measurements. As shown in Figure 2 the HTlc precursors show similar platelet-like morphology, but the particle sizes differed considerably. Small platelets were obtained for PdMgAl (Fig 2C) and PdZnAl (Fig. 2A). The thickness of the platelets is in the low nanometer range, while the lateral dimension is approximately around 250 nm or below. Although for PdMgAl and PdMgGa samples same synthesis conditions were applied the lateral size of the PdMgGa platelets is increased to 0.4-1 μm. The PdMgGa and PdMgAl platelets exhibit sandrose morphology, while the PdZnAl platelets are randomly oriented. No large Pd agglomerates were detected by SEM outside the platelets and also EDX mapping suggests a homogenous metal distribution for all samples (not shown).

3.2. Reducibility of HTlc precursors and IMC formation

3.2.1 TPR and MS measurements

TPR experiments were performed in order to study the IMC formation and monitor the reduction process. All TPR profiles can be separated into three regions: a room temperature reduction (RTR), a low temperature reduction (LTR, < 300 °C) and high

temperature reduction region (HTR, > 300 °C). RTR contains any initial hydrogen consumption detected upon switching to reducing atmosphere at room temperature (before the heating ramp was started). Figure 3 includes the LTR and HTR processes, only. The reduction from Pd^{2+} to metallic Pd^0 normally occurs in the RTR or LTR regime, at temperature lower than ca. 150 °C. Quantification of the degree of reduction from the hydrogen consumption turned out to be complex for these samples. Metal Pd particles form hydrides and transfer spillover hydrogen to the support material; both phenomenal lead to higher hydrogen consumption than expected for stoichiometric Pd^{2+} reduction.[21] The PdH_x phase is not stable during heating and decomposes at higher temperatures, producing a negative peak in the TPR profile. In the HTR regime hydrogen consumption due to partial reduction of reducibile oxides overlaps with further H_2 consumption due to conversion of CO_2, which is released as a decomposition product of the interlayer carbonate ions. As a matter of fact, CO and CH_4 have been detected by MS during LTR and HTR (Figure S 2). These results provide an evidence that evolved CO_2 is not completely removed from the catalyst bed, but varying fractions undergo rWGS and methanation at the surface of the metallic nanoparticles. Taking into account all these phenomena, the hydrogen consumption was always considerably higher than expected for stoichiometric reduction of the metal cations. Apparently, hydride formation, spillover hydrogen, and CO_2 conversion dominate the consumption of H_2: therefore, the TPR data shown in Figure 3 will be discussed in a semi-quantitative manner, i.e. by comparison of the TCD peak integrals of the different samples in the different temperature regimes.

As expected, no hydrogen consumption was observed in the RTR and LTR regions for the Pd-free samples. For the Pd containing precursors, the profiles in this region are different. Hydrogen consumption in both RT and LT regions were observed for PdMgGa and PdMgAl samples, while for PdZnAl sample H_2 uptake was detected only at LT. This suggests that in the former samples two different Pd^{2+} species were present, one easily and one harder to reduce. The main LTR peaks are found at 82, 109 and ca. 80 °C for PdZnAl, PdMgGa and PdMgAl, respectively, which are relatively high values for the reduction of Pd^{2+}. From this observation, the RTR peak can be assigned to reduction of PdO-like species not incorporated into the HTl lattice, while the LTR peaks are due to reduction of HTl-lattice Pd^{2+} cations. This assumption is consistent with XANES measurements discussed below. Furthermore, Pd hydride decomposition is observed only for PdMgAl (small negative peak around 150°C). Additional LTR uptake was observed for PdZnAl at 247 °C. It is known that ZnO can be reduced in the presence of metal Pd at such mild temperatures to form the IMC PdZn. [13, 21]

Since the above mentioned LTR peak is absent for the Pd-free precursor, it is assigned to reduction of ZnO with the consequent IMC formation (although small amounts of CH_4 were detected at this temperature). No further peaks are detected in the LTR region for PdMgAl and PdMgGa samples. In PdMgAl there are no other reducible species. in PdMgGa this observation indicates that the IMC formation takes place at higher temperature; therefore, the process cannot be accurately studied by TPR, because of the overlap with CO_2 conversion in the higher temperature regime, see S 2.

Coming to the HTR regime, hydrogen consumption was detected for all precursors, also for the Pd-free MgGa and ZnAl, except for MgAl. At these temperatures, partial reduction of the reducible oxides is expected also in the absence of Pd. Starting from PdZnAl and ZnAl, HTR consumption peaks having a similar integral area were observed at approximately the same temperature (537 °C and 549 °C). No traces of CO, or CH_4 were noticed by MS at that temperature (S 2);as a consequence, the peaks are assigned to reduction of the ZnO-component of the support. For MgGa and PdMgGa, the presence of Pd leads to an increase of the total HTR hydrogen consumption and to a down-shift in temperature from 459 to 421 °C. In both cases, CO was detected by MS in this temperature region. Thus, at sufficiently high temperature CO_2 deriving from decarboxylation of the interlayer carbonate anions undergoes rWGS on the reducible oxides.[22] For PdMgGa the hydrogen uptake due to rWGS and support reduction overlaps with IMC formation (Figure S 2).

Only the non reducible MgAl sample does not show any significant hydrogen consumption over the whole temperature range. Addition of Pd to this sample induced an uptake of hydrogen at 413 °C; correspondingly, CH_4 was detected by MS (Figure S 2C). Therefore, it is concluded that CO_2 deriving from decomposition of the interlayer carbonates is converted to CH_4. TPR and MS data provide a first evidence that the catalytic properties of Pd have been markedly modified by formation of IMCs. While PdMgAl (where no IMC is formed) was found to be active in methanation, PdMgGa converts CO_2 in the rWGS to CO at comparable conditions. The HTR hydrogen conversion of PdZnAl can be completely ascribed to the reducibility of the support material. From the TPR results, the reduction temperatures for IMC formation were estimated to 250 °C for PdZnAl and 500 °C for PdMgGa. The PdMgAl reference sample was reduced at 250 °C.

3.2.2 XANES measurements

XANES measurements were carried out to gain more insight into the Pd speciation in the precursor and in the RTR and LTR events. Since TPR measurements suggested the presence of two Pd^{2+}-species in PdMgAl and PdMgGa, different reference materials were used.

Commercial PdO was chosen as reference material for segregated Pd^{2+} species in the precursor, which is not incorporated in to the HTl lattice. Pd^{2+} in PdO is characterized by a square planar coordination. On the contrary, when incorporated into the hydrotalcite lattice Pd^{2+} assumes a octahedral coordination. The low-spin d^8 electronic configuration of Pd^{2+} makes regular octahedral coordination unstable with respect to large tetragonal elongations. Octahedral coordination of Pd^{2+} with oxygen was obtained in a high-pressure phase of PdO at 12 GPa.[23] Moreover, octahedral environment was also observed for Pd cations having a higher oxidation state. For instance, Zn_2PdO_4 is a compound where Pd^{4+} has regular octahedral symmetry in the cubic spinel structure [24], while in $LaPdO_3$ Pd^{3+} has a distorted perovskite structure that stabilizes the trivalent ion in octahedral coordination [25].

The XANES spectra of the HTlc precursors are shown in Figure 4; both in the unreduced state and after treatment at 50 °C in hydrogen, i.e. at a temperature where RTR has already occurred, but low enough not to trigger LTR. XANES spectra of PdO as reference for segregated Pd^{2+} species before RTR and of metallic Pd for the state after RTR were included. The intensity ratio of the white line and the first feature of the XANES of PdZnAl HTlc is significant different from that of PdO and similar to that reported for $LaFe_{0.95}Pd_{0.05}O_3$ where Pd exhibits a distorted octahedral coordination.[26] Changing to reducing atmosphere did not induce a change of the XANES of PdZnAl, which is in agreement with the TPR experiment that did not show any RT reduction. Therefore, we assume that in this sample Pd^{2+} is fully incorporated into the HTl structure and not available for reduction to metallic Pd below 50 °C. This spectrum was taken as a reference for HTlc incorporated Pd^{2+} in the linear combination analysis of the other samples (as shown in Figure 4B and C). PdMgAl and PdMgGa HTlc's showed a certain degree of RT reduction in the TPR; also the XANES spectra changes upon H_2 reduction at 50°C (Figure 4), although only for PdMgAl do the near-edge features look almost identical to those of metallic Pd^0. The PdMgGa sample is apparently more stable and changes only slightly. Accordingly, analysis reveals that 67% of Pd^{2+} is present in octahedral coordination, while in case of PdMgAl only 61% of Pd^{2+} is incorporated. Correspondingly, a stronger LTR peak was observed for PdMgGa.

3.3. Properties of the ex-HTlc samples after reduction

The XRD patterns of the reduced samples presented in Figure 1 contain only broad modulations of the background suggesting poor crystallinity and small crystallite sizes. In particular, after reduction at 250 °C PdMgAl is amorphous (Figure 1F) and only heating to 500 °C leads to significant growth of XRD peaks due to poorly crystalline MgO and $MgAl_2O_4$ (not shown). Formation of periclase and spinel phases was also observed for

PdMgGa after reduction at 500 °C (Figure 1B). The PdZnAl sample showed very weak and broad peaks due to ZnO after reduction at 250 °C (Figure 1D). The XRD data are in agreement with HRTEM analysis of the phases of the support.

Because the metallic component could not be identified by means of XRD, due to both the small total amount and low crystallite size, XANES and HRTEM were applied for phase identification. Figure 5 shows the XANES spectra of the reduced precursors at the reduction temperatures elaborated by the TPR experiment. Palladium foil, bulk Pd_2Ga and PdZn are shown as reference materials. In general, lower amplitudes of the first EXAFS oscillations were observed for the nanoparticulate samples, in particular for PdZnAl. Nevertheless the spectra show a high agreement and resembled those of the associated references.

TEM revealed that the platelet-like morphology of the HTlc precursor was retained after reduction and all catalysts showed spherical particles distributed on the platelets as presented in Figure 6-8. HRTEM images were used to determine the net plane distances and plane angles by FFT. Figure 6 shows the PdMgAl sample after reduction at 500 °C. In STEM mode homogeneous and small-sized Pd nanoparticles on $MgAlO_x$ support were observed and HRTEM investigations confirming the presence of metallic Pd (ICDD 65-6174). Reduction of PdMgGa also yielded supported nanoparticles as presented in Figure 7. The corresponding power spectrum, shown in Figure 7, allowed identification of the intermetallic Pd_2Ga phase (ICDD 65-1511). In agreement with XRD data, partially crystalline MgO and $MgGa_2O_4$ were present as oxidic support. However, for PdZnAl two different Pd-Zn IMCs were identified after reduction at 250 °C (Figure 8). The crystal planes $(1\bar{1}1)$ and (111) of PdZn (ICDD 6-620) were identified with the characteristic acute angle of 65° along the $[\bar{1}01]$ zone axis. Additionally, nanoparticles with a core-shell structure were present. The phase in the core was identified as Pd_2Zn (circled area, ICDD 6-629) surrounded by an ordered shell of ZnO. This arrangement suggests that Pd_2Zn might be an intermediate of the reduction of PdZnAl. ZnO seems to have segregated from the oxide support to encapsulate the metal core by strong metal support interaction and supply further Zn atoms for IMC formation through the reactive Pd-ZnO and Pd_2Zn-ZnO interfaces, finally resulting in formation of PdZn. The average particle sizes were obtained from projected areas of the metal particles and were 1.8, 2.2 and 6.1 nm for PdZnAl, PdMgAl and PdMgGa HT, respectively. The considerably large size of the Pd_2Ga particles can be explained by the higher reduction temperature that was necessary to form the IMC. The corresponding size distributions are shown in S 3.

FT-IR spectroscopy of adsorbed CO was adopted to investigate the surface properties of the metallic Pd, PdZn and Pd_2Ga components in PdMgAl, PdZnAl and PdMgGa. The FT-

IR spectra of CO adsorbed at room temperature on the three samples are shown in Figure 9 as a function of CO coverage. Several IR absorption bands were observed in the range of 2100-2000 cm^{-1} and 1970-1800 cm^{-1}. These IR absorption bands are characteristic of linearly and multiply bonded CO on Pd^0 atoms, respectively [27]. As reported by Kovnir et al. [28] and Conant et al. [14], no or very few multiple bonded carbonyl species should be observed for Pd-Ga and Pd-Zn intermetallic compounds. Indeed, mainly on-top coordinated CO species, characterized by IR absorption bands at 2080 cm^{-1} and 2050 cm^{-1}, were observed for PdMgGa and PdZnAl, as shown in Figure 9A and B. In contrast, CO adsorption on PdMgAl sample revealed a much larger population of multiply bonded sites compared to linearly coordinated CO (Figure 9C). At low CO coverage the band of linearly coordinated CO was observed at 2020 cm^{-1} , which is relatively low, but still in the characteristic range. According Prinetto et al. [29], the frequency red shift originates from CO adsorption on Pd sites, whose electronic properties are modified by interaction with basic support species. With increasing CO coverage, an additional band at 2080 cm^{-1} gains intensity and slightly shifts to higher wavenumbers due to increased dipole-dipole coupling of the neighboring CO groups.

Summarizing this part, small particles of the IMCs have been obtained from HTlc precursors with at least partial Pd^{2+} incorporation on octahedral sites in the cationic slabs. Upon reduction in hydrogen, metallic Pd segregated from the precursors at low temperature and, as the reduction temperature increases, IMC particles are formed. For PdZnAl the IMC PdZn is formed at 250 °C probably via a Pd_2Zn intermediate stage. The average particle size is about 1.8 nm. Pd_2Ga formed from PdMgGa at higher temperature (500 °C); the average particle size is larger (about 6.1 nm). Compared to the monometallic Pd particles oobtained on PdMgAl, the adsorptive properties of the IMC particles are strongly modified, suggesting differences in catalytic properties.

3.4. Catalytic properties of IMCs

3.4.1 Methanol synthesis

Activity versus time-on-stream data for methanol synthesis and rWGS at 250 °C is shown in Figure 10 for all Pd based catalysts. After a 5 hour stabilization period, all catalysts show only very slow loss of activity with time-on-stream. PdMgGa and PdZnAl showed similar steady-state activities for methanol synthesis of 18.7 and 17.6 µmol/(g_{cat}·min), respectively. These activities amounted to nearly 30 times the methanol synthesis activity of PdMgAl (0.65 µmol/(g_{cat}·min)). In contrast to this difference, the rWGS of all catalysts were within a similar range, with PdMgGa (27.8 µmol/(g_{cat}·min)) being twice as active as PdMgAl and PdZnAl with 14.3 and 13.5 µmol/(g_{cat}·min), respectively. These results are consistent with those of

Iwasa et al. [30] and Fujitani et al. [31], who showed that Pd supported on ZnO and Ga_2O_3 possessed significant methanol synthesis activity, whereas unsupported Pd and Pd on inert SiO_2 were almost inactive for methanol synthesis. Additionally, the results of Iwasa showed far less significant differences in rWGS rates on these catalysts. A similar observation about rWGS activities can be made for the catalysts studied in this work. From this observation it can be concluded that free Pd may be responsible for the rWGS activity, whereas the intermetallic sites lead to methanol formation. However, Iwasa et al. [30] had shown that the rWGS activity of Pd/ZnO decreases by only 40% upon the complete conversion of Pd into a PdZn alloy. It is therefore possible that the intermetallic surfaces behave similarly to Cu, in that they possess sites for both methanol synthesis and rWGS.

In order to correctly compare the intrinsic activities and apparent activation energies for the Pd catalysts with those of a more active CuZnAl catalyst, which was also prepared from a single phase HTlc precursor, the space velocity had to be varied. When all catalysts are compared at 250 °C and a space velocity of 10 mmol/(g_{cat}·min) , the Cu based catalyst shows a CO_2 conversion of 5% and a mass normalized methanol synthesis rate that is 6 times that of the bimetallics, which each show less ~1% CO_2 conversion. At these conditions, PdMgGa (0.51 min^{-1}) appears twice as intrinsically active (TOF) as PdZnAl (0.12 min^{-1}) and is more active than the CuZnAl catalyst (0.39 min^{-1}). PdZnAl shows a similar methanol selectivity to that of CuZnAl (60%) and is more selective that PdMgGa (47%). According to several investigators, the water produced during methanol synthesis and rWGS acts to inhibit methanol synthesis on Cu. [32, 33] The concentration of this water is directly dependent on the CO_2 conversion. In that respect, the CuZnAl catalyst is exposed to 5 times more water than the IMC catalysts when tested at the same gas space velocity. To take the effects of water inhibition into account, the space velocity for CuZnAl was raised to 93 mmol/(g_{cat}·min), resulting in a CO_2 conversion of 1.3%, i.e. in the same range as for the IMC catalysts at lower space velocities. At these conditions, the methanol TOF increased to 1.3 min^{-1}, and is 4-12 times higher than that of the IMCs (Table 2). Furthermore, at these conditions CuZnAl shows a significantly higher selectivity to methanol synthesis (82%) as compared to the IMCs. It should be noted however, that the intrinsic activities of the IMCs are still two orders of magnitude higher than of PdMgAl.

The comparison of apparent activation energies between Cu- and Pd-based catalysts results in an intuitive understanding to the effect of IMC formation on reactivity. The Arrhenius plots for methanol synthesis and rWGS are shown in Figure 11 for Pd-based catalysts tested at a space velocity of 10 mmol/(g_{cat}·min) and CuZnAl at 93 mmol/(g_{cat}·min). It is interesting to

note that the activation energy for methanol synthesis decreases from 72 kJ/mol in PdMgAl to 68 kJ/mol in PdZnAl and 59 kJ/mol in PdMgGa upon the substitution of Al with Ga and Mg with Zn respectively, and approaches 54 kJ/mol as measured for CuZnAl. Similarly for rWGS, substitution causes an increase in the apparent activation energy from 69 kJ/mol in PdMgAl to 94 kJ/mol and 82 kJ/mol for PdZnAl, PdMgGa respectively, in the direction of CuZnAl (122 kJ/mol). The results suggest that the reactivity of Pd in methanol synthesis and rWGS approaches that of Cu upon substitution of irreducible species with Zn and Ga. In particular, these extraordinary differences in reactivity correspond to the formation of PdZn and Pd_2Ga IMCs upon reduction of PdZnAl and PdMgGa respectively and the presence of only pure Pd upon reduction of PdMgAl, as evidenced by the aforementioned characterization results. The similarity of the catalytic properties of PdZn and Cu has been reported in literature and was attributed to the similar electronic structure. Both exhibits similar valence electron densities of states (DOS) as confirmed by DFT, UPS and XPS.[34-37]

3.4.2. Steam reforming of methanol

The catalytic activities of the Pd-based catalysts derived from HTlc precursors in SRM tests are summarized in Table 3. For all tested catalysts the main products were H_2, H_2O, CO and CO_2. Other reaction products such as formaldehyde or dimethylether were not observed. The PdZnAl and PdMgGa catalysts showed similar overall activity (9.5% methanol conversion), while the PdMgAl catalyst was somewhat less active (7% methanol conversion). The PdZnAl catalyst possessed the highest hydrogen yield (660 µmol/(g_{cat}·min)) of all catalysts tested, and this hydrogen yield was 23% and 75% higher than those of PdMgGa and PdMgAl respectively (Figure 12). In terms of intrinsic activity for hydrogen production, the PdZnAl and PdMgGa were 2 and 6 times respectively more active than PdMgAl. The hydrogen selectivities of PdMgGa and PdMgAl were significantly lower (70%) than that of PdZnAl (87%).

While the reactivity of methanol on PdMgAl and PdMgGa is almost entirely dominated by methanol decomposition, PdZnAl shows considerable SRM activity (S_{CO2}=61%). Iwasa et al. [7] have attributed this CO_2 selectivity to the formation PdZn intermetallic phases during reduction of Pd/ZnO. However, the CO_2 selectivities observed by Iwasa. et al were near 95% and thereby similar to those observed on CuZn based catalysts. It should be noted that the PdZn particles observed by Iwasa et al. [8] were large enough to produce rather sharp XRD peaks and where therefore far larger than the particles obtained in this work. It may therefore be possible that, in reaction conditions, the smaller particles decompose partially to yield

metallic Pd (which is not selective), or that the methanol decomposition reaction is structure sensitive, and occurs faster on smaller particles. In accordance with the latter statement, Karim et al [38], using TEM analysis, found a positive correlation between the number of small particles (<1.5nm) and decreasing selectivity towards CO_2 on Pd/ZnO catalysts.

Iwasa [8] and more recently, Haghofer [9] have shown that Pd supported on Ga_2O_3 is also very selective to MSR with CO_2 selectivities above 80% , and have attributed this high selectivity to the formation of Pd-Ga IMCs. However, for the PdMgGa sample investigated herein the CO_2 selectivity (16%) is only somewhat higher than that of the PdMgAl (6%) catalyst, in which no IMCs are formed. Through in situ IR spectroscopy on Pd/Ga_2O_3, Haghofer et al [20] have shown that the intermetallic Pd-Ga surface is not entirely stable during SRM at 207 °C, and that metallic Pd forms on the surface, as evidenced by the presence of bridge-bonded CO. At the higher temperatures (250 °C) used in this study, such surface decomposition may occur to a greater extent and leave a higher fraction of exposed Pd, thus leading to lower CO_2 selectivities. It should be noted that the promotional effect of Pd_2Ga formation on the selectivity is far more evident during methanol synthesis (as described previously) as compared to steam reforming. To that end, the higher hydrogen pressures and virtual absence of water during methanol synthesis may ensure the stability of the Pd_2Ga intermetallic surface responsible for the enhanced selectivity. In contrast, the presence of large concentrations of water during SRM may lead to the decomposition of this surface into metallic Pd and Ga_2O_3. Corresponding to its lower formation temperature, the PdZn IMC seems to possess a greater stability in less reducing atmospheres than Pd_2Ga and the beneficial intrinsic catalytic properties prevail to a greater extent in the PdZnAl catalyst.

Conclusion

A flexible synthetic approach for the synthesis of nanoparticles of intermetallic compounds has been presented. PdZn (1.8 nm) and Pd_2Ga (6.1 nm) nanoparticles could be obtained from HTlc precursor with a homogeneous distribution of Pd and intimate interaction with the other reducible metal species. At a degree of substitution of 1 mol%, full incorporation of Pd^{2+} in the HTlc lattice has been confirmed for PdZnAl, while in PdMgAl and PdMgGa the majority of Pd^{2+} was incorporated. Upon reduction in hydrogen, metallic Pd segregated from the precursors at low temperature and for PdZnAl the PdZn IMC is formed at 250 °C, probably via a Pd_2Zn intermediate stage. Formation of Pd_2Ga IMC in PdMgGa requires 500 °C. In comparison with the analogous PdMgAl sample, which does not contain a second reducible species and yields monometallic Pd nanoparticles, the CO adsorption properties as well as the

catalytic properties have markedly changed through formation of the IMCs. Improved activities and selectivities in SRM and methanol synthesis from CO_2 have been observed. This effect is larger for CO_2 hydrogenation than for SRM, and for the PdZn-based than for the Pd_2Ga-based catalyst. These differences are probably related to the different sensitivity of the IMC surface against decomposition into Pd metal and oxide. Under steady state conditions our Pd-based IMC catalysts are inferior to Cu/ZnO reference systems. Nevertheless, the potential of these materials for SRM operation at higher temperature and under changing reaction conditions like on-off operations remains to be investigated. Also the stability of the IMC surface under different conditions needs further investigation.

Acknowledgement

The authors thank Edith Kitzelmann (XRD), Gudrun Auffermann (ICP-OES), Gisela Lorenz (BET), and Stafania Sabatino (FT-IR) for their help with various characterizations. Gregor Wowsnick (bulk Pd_2Ga), Matthias Friedrich and Marc Armbrüster (bulk PdZn) and Stefanie Kühl (CuZnAl) are acknowledged for providing the used reference samples. Paul Scherer Institute (SLS, SuperXAS) is acknowledged for allocation of beamtime. Olga Safonova, Maarten Nachtegaal, Andrey Tarasov and Patrick Kast are acknowledged for their assistance during beamtime. Many thanks to the COST Action CM0904 "Network for Intermetallic Compounds as Catalysts in the Steam Reforming of Methanol" for providing these multi-collaboration.

Supporting Information Available:

Supporting Information includes the synthesis recipe of the CuZnAl reference sample and synthesis protocols of the Pd based precursor. Furthermore, MS profiles of the reduction processes (Figure S 2) and the particle size distribution are included (Figure S 3).

[1] G. A. Olah, A. Goeppert, G. K. S. Pakash, Beyond Oil and Gas: The Methanol Economy, Wiley-VCH Verlag GmbH & Co. KGaA, Weinheim, 2006.

[2] R. Schlögl, Chemsuschem 2010, 3, 209-222.

[3] P. J. de Wild, M. J. F. M. Verhaak, Catalysis Today 2000, 60, 3-10.

[4] F. Joensen, J. R. Rostrup-Nielsen, Journal of Power Sources 2002, 105, 195-201.

[5] R. Schögl, Energy Storage Materials, Walter de Gruyter, Berlin, 2012.

[6] L. Guczi, A. Erdôhelyi, Catalysis for Alternative Energy Generation, 1st ed., Springer 2012.

[7] N. Iwasa, S. Masuda, N. Ogawa, N. Takezawa, Applied Catalysis A: General 1995, 125, 145-157.

[8] N. Iwasa, T. Mayanagi, N. Ogawa, K. Sakata, N. Takezawa, Catalysis Letters 1998, 54, 119-123.

[9] A. Haghofer, K. Föttinger, F. Girgsdies, D. Teschner, A. Knop-Gericke, R. Schlögl, G. Rupprechter, Journal of Catalysis 2012, 286, 13-21.

[10] S. Penner, H. Lorenz, W. Jochum, M. Stöger-Pollach, D. Wang, C. Rameshan, B. Klötzer, Applied Catalysis A: General 2009, 358, 193-202.

[11] H. Lorenz, S. Penner, W. Jochum, C. Rameshan, B. Klötzer, Applied Catalysis A: General 2009, 358, 203-210.

[12] C. Rameshan, W. Stadlmayr, C. Weilach, S. Penner, H. Lorenz, M. Hävecker, R. Blume, T. Rocha, D. Teschner, A. Knop-Gericke, R. Schlögl, N. Memmel, D. Zemlyanov, G. Rupprechter, B. Klötzer, Angewandte Chemie International Edition 2010, 49, 3224-3227.

[13] K. Föttinger, J. A. van Bokhoven, M. Nachtegaal, G. n. Rupprechter, The Journal of Physical Chemistry Letters 2011, 2, 428-433.

[14] T. Conant, A. M. Karim, V. Lebarbier, Y. Wang, F. Girgsdies, R. Schlögl, A. Datye, Journal of Catalysis 2008, 257, 64-70.

[15] A. Ota, M. Armbrüster, M. Behrens, D. Rosenthal, M. Friedrich, I. Kasatkin, F. Girgsdies, W. Zhang, R. Wagner, R. Schlögl, The Journal of Physical Chemistry C 2010, 115, 1368-1374.

[16] K. Kovnir, J. Osswald, M. Armbruster, D. Teschner, G. Weinberg, U. Wild, A. Knop-Gericke, T. Ressler, Y. Grin, R. Schlogl, Journal of Catalysis 2009, 264, 93-103.

[17] X. Duan, D. G. Evans, Layered Double Hydroxides, Springer-Verlag, Berlin, Heidelberg, 2006.

[18] C. Forano, T. Hibino, F. Leroux, C. Taviot-Gueho, in Handbook of Clay Science (Eds.: F. Bergaya, B. K. G. Theng, G. Lagaly), Elsevier, 2006, pp. 1021-1095.

[19] F. Cavani, F. Trifirò, A. Vaccari, Catalysis Today 1991, 11, 173-301.

[20] M. Behrens, I. Kasatkin, S. Kühl, G. Weinberg, Chemistry of Materials 2009, 22, 386-397.

[21] N. Iwasa, T. Mayanagi, W. Nomura, M. Arai, N. Takezawa, Applied Catalysis A: General 2003, 248, 153-160.

[22] W. Jochum, S. Penner, R. Kramer, K. Föttinger, G. Rupprechter, B. Klötzer, Journal of Catalysis 2008, 256, 278-286.

[23] A. G. Christy, S. M. Clark, Physical Review B 1995, 52, 9259-9265.

[24] G. Demazeau, I. Omeran, M. Pouchard, P. Hagenmuller, Materials Research Bulletin 1976, 11, 1449-1452.

[25] S.-J. Kim, S. Lemaux, G. Demazeau, J.-Y. Kim, J.-H. Choy, Journal of Materials Chemistry 2002, 12, 995-1000.

[26] A. Eyssler, P. Mandaliev, A. Winkler, P. Hug, O. Safonova, R. Figi, A. Weidenkaff, D. Ferri, The Journal of Physical Chemistry C 2010, 114, 4584-4594.

[27] N. Sheppard, C. De La Cruz, Catalysis Today 2001, 70, 3-13.

[28] K. Kovnir, M. Armbrüster, D. Teschner, T. V. Venkov, F. C. Jentoft, A. Knop-Gericke, Y. Grin, R. Schlögl, Science and Technology of Advanced Materials 2007, 8, 420-427.

[29] F. Prinetto, M. Manzoli, G. Ghiotti, M. d. J. Martinez Ortiz, D. Tichit, B. Coq, Journal of Catalysis 2004, 222, 238-249.

[30] N. Iwasa, H. Suzuki, M. Terashita, M. Arai, N. Takezawa, Catalysis Letters 2004, 96, 75-78.

[31] T. Fujitani, M. Saito, Y. Kanai, T. Watanabe, J. Nakamura, T. Uchijima, Applied Catalysis A: General 1995, 125, L199-L202.

[32] W. Wang, S. Wang, X. Ma, J. Gong, Chemical Society Reviews 2011, 40, 3703-3727.

[33] T. Inui, T. Takeguchi, Catalysis Today 1991, 10, 95-106.

[34] A. P. Tsai, S. Kameoka, Y. Ishii, Journal of the Physical Society of Japan 2004, 73, 3270-3273.

[35] A. Bayer, K. Flechtner, R. Denecke, H.-P. Steinrück, K. M. Neyman, N. Rösch, Surface Science 2006, 600, 78-94.

[36] K. M. Neyman, K. H. Lim, Z.-X. Chen, L. V. Moskaleva, A. Bayer, A. Reindl, D. Borgmann, R. Denecke, H.-P. Steinruck, N. Rosch, Physical Chemistry Chemical Physics 2007, 9, 3470-3482.

[37] Z.-X. Chen, K. M. Neyman, A. B. Gordienko, N. Rösch, Physical Review B 2003, 68, 075417.

[38] A. Karim, T. Conant, A. Datye, Journal of Catalysis 2006, 243, 420-427.

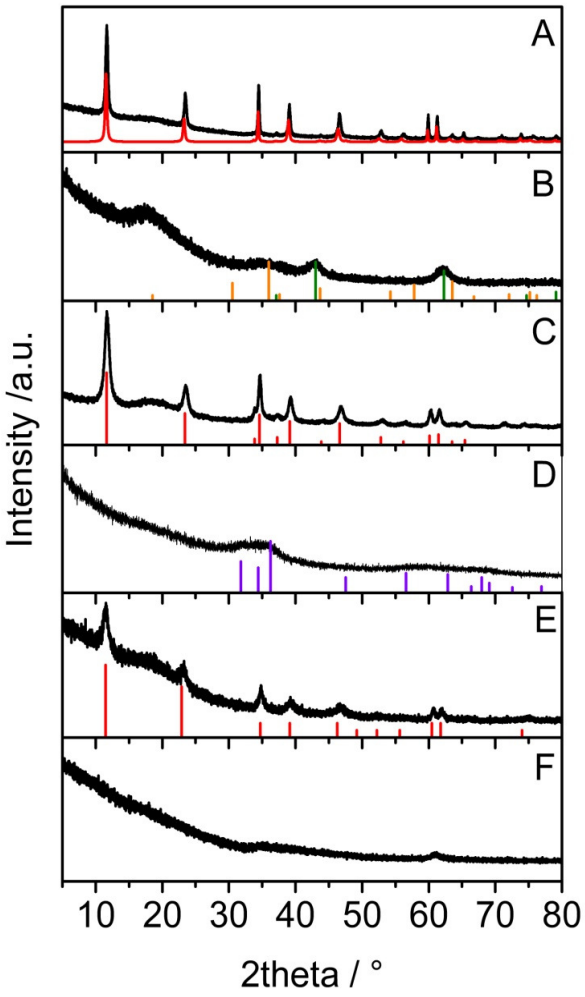

Figure 1: XRD patterns of (A) PdMgGa HTlc and simulated MgGa HTlc precursor; (B) ex-PdMgGa HTlc after reduction at 500 °C, ICDD 1-1235 MgO (green), ICDD 10-113 $MgGa_2O_4$ (orange); (C) PdZnAl HTlc precursor and ICDD 38-486 $Zn_6Al_2(OH)_{16}CO_3{\cdot}4\ H_2O$; (D) ex-PdZnAl HTlc after reduction at 250 °C, ICDD 36-1451 ZnO (violet); (E) PdMgAl HTlc precursor and ICDD 14-191 $Mg_6Al_2(OH)_{16}CO_3{\cdot}4\ H_2O$; (F) ex-PdMgAl HTlc after reduction at 250 °C.

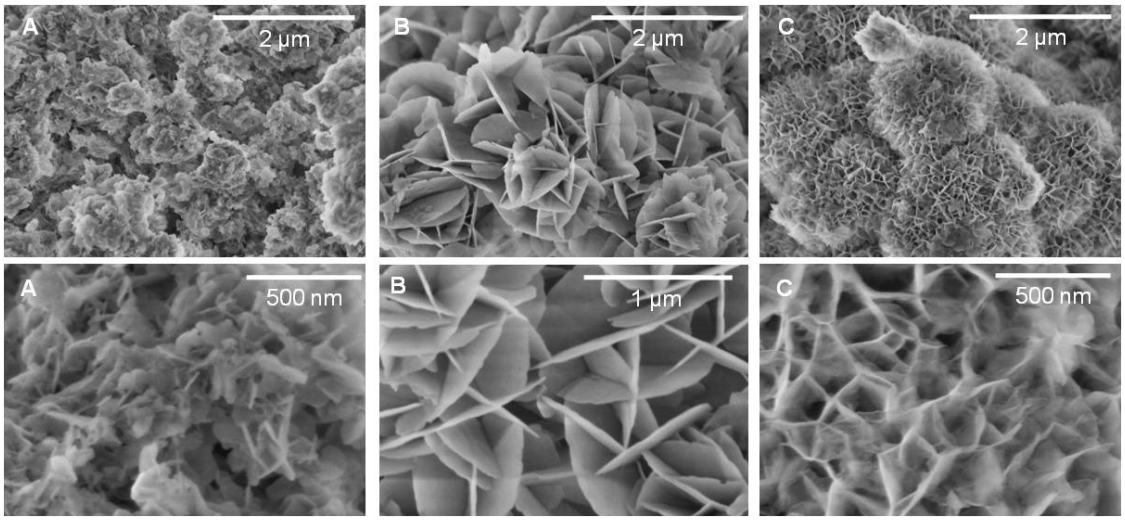

Figure 2: SEM images of (A) PdZnAl (B) PdMgGa and (C) PdMgAl HTl precursor.

Bottom parts show a magnification of top parts.

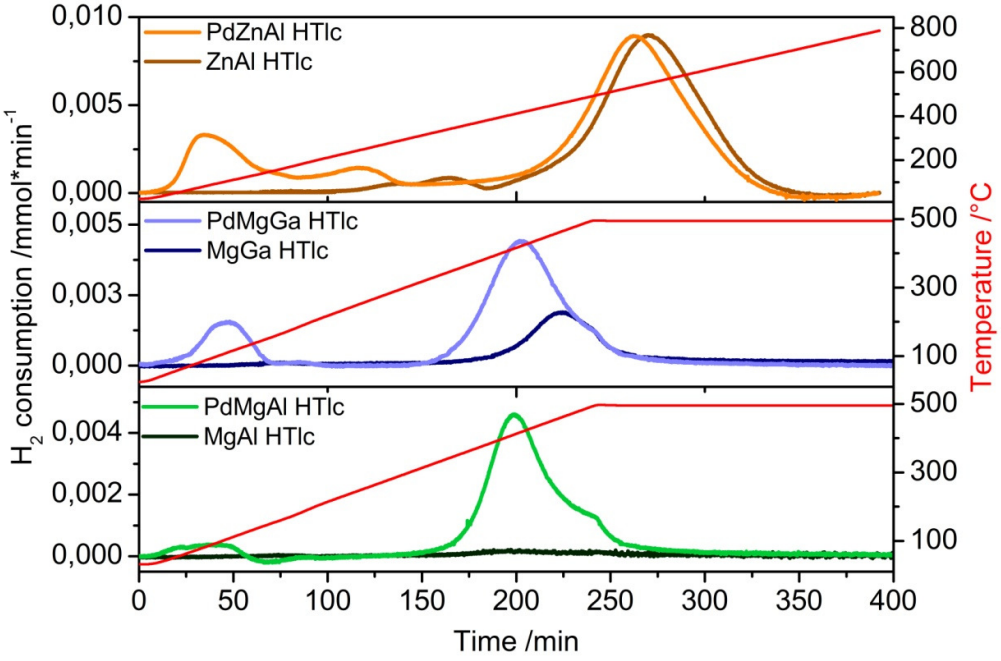

Figure 3: TPR profiles of Pd doped and undoped Hydrotalcite-like precursors in 5% H_2/Argon.

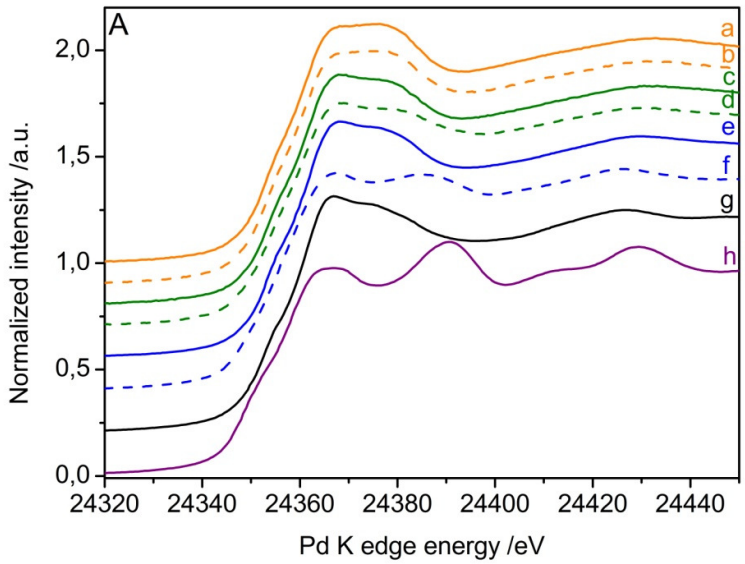

Figure 4A: XANES spectra PdZnAl at RT/He (a) and 50 °C/H_2 (b), PdMgGa at RT/He (c) and 50 °C/H_2 (d), PdMgAl at RT/He (e) and 50 °C/H_2 (f), PdO (g) and Pd foil (h) reference.

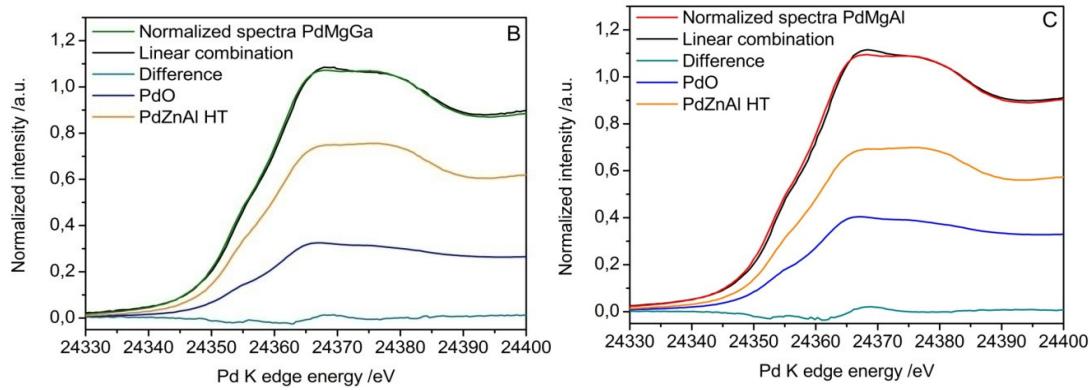

Figure 4B+C: Linear combination fit of the XANES spectra of PdMgGa and PdMgAl precursor, by using PdO and PZnAl as references for Pd^{2+} in square planar and octahedral coordination, respectively.

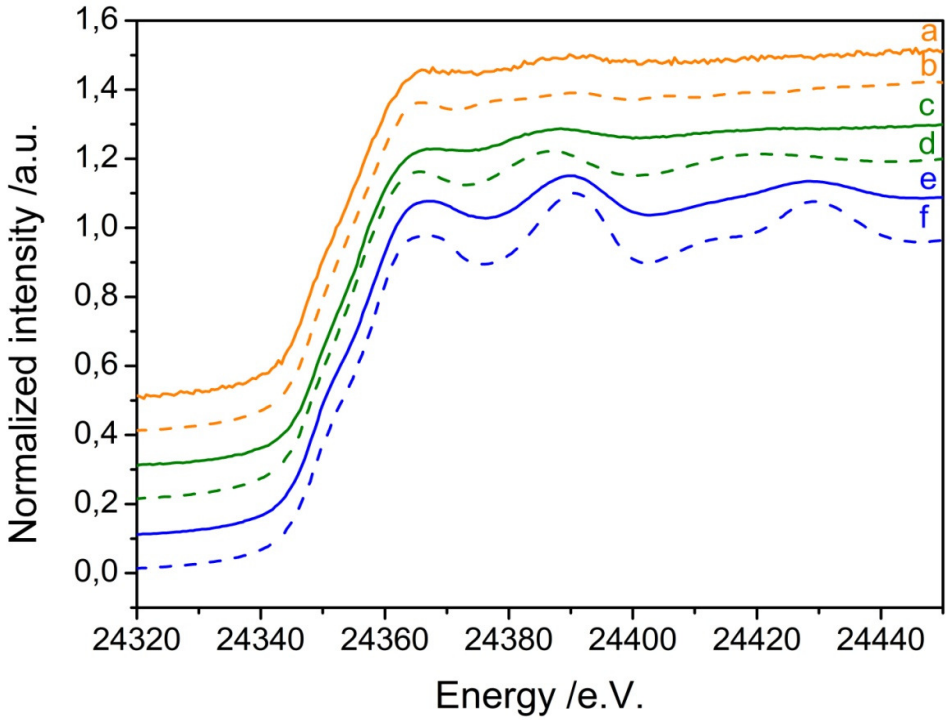

Figure 5: XANES spectra of (a) PdZnAl reduced at 250 °C and (b) bulk PdZn, (c) PdMgGa reduced at 500 °C and (d) bulk Pd_2Ga, (e) PdMgAl reduced 250 °C and (f) Pd foil.

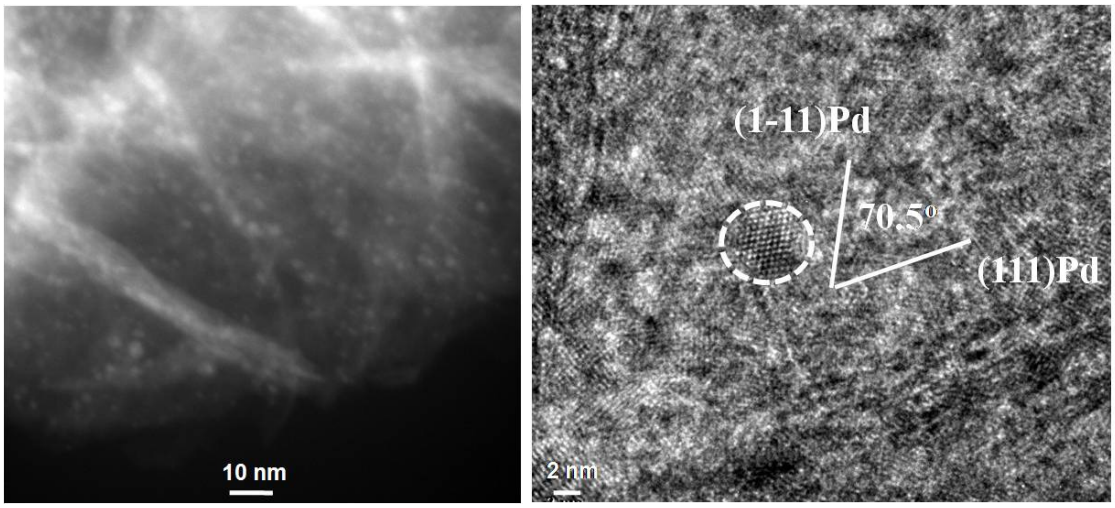

Figure 6: TEM images of PdMgAl after reduction at 500 °C in 5%H_2/Argon.

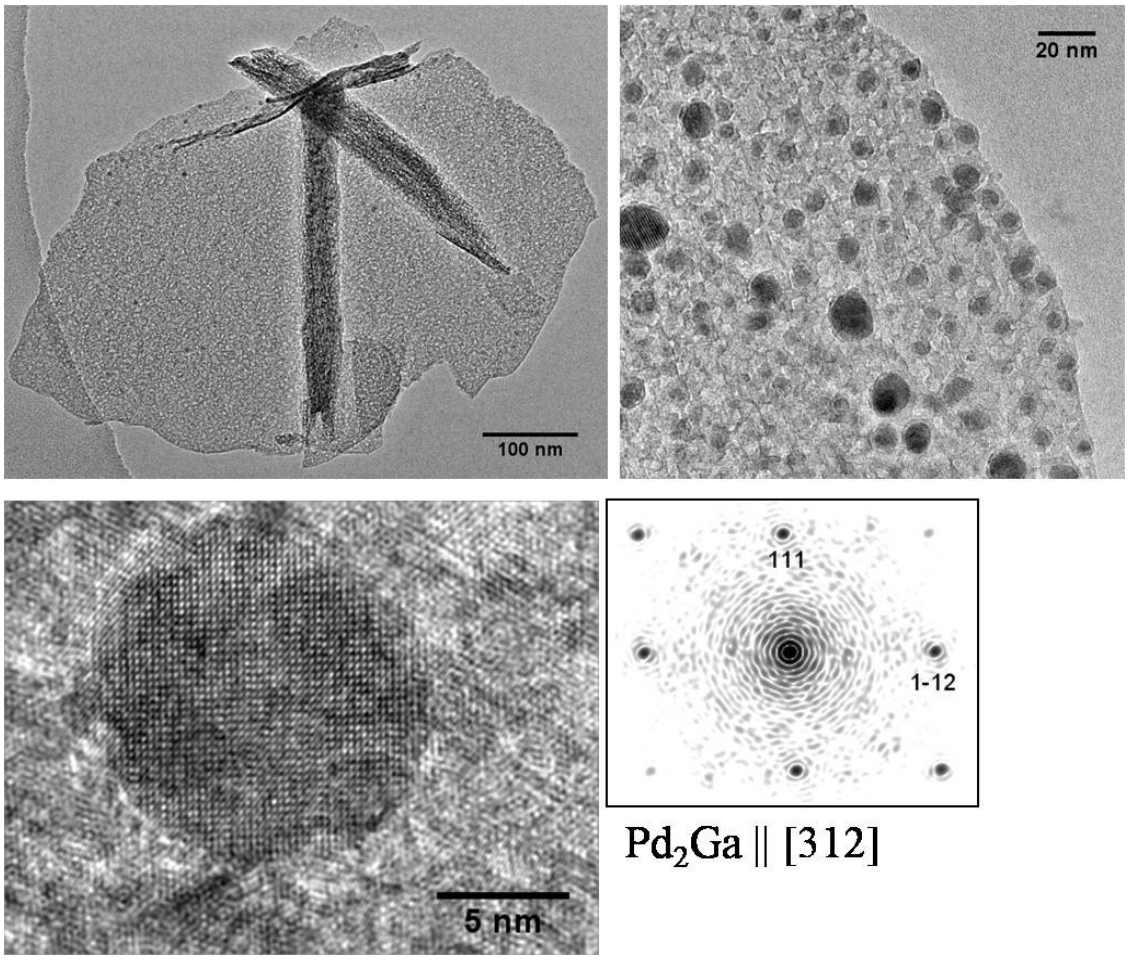

Figure 7: TEM images of PdMgGa after reduction at 500 °C in 5%H_2/Argon.

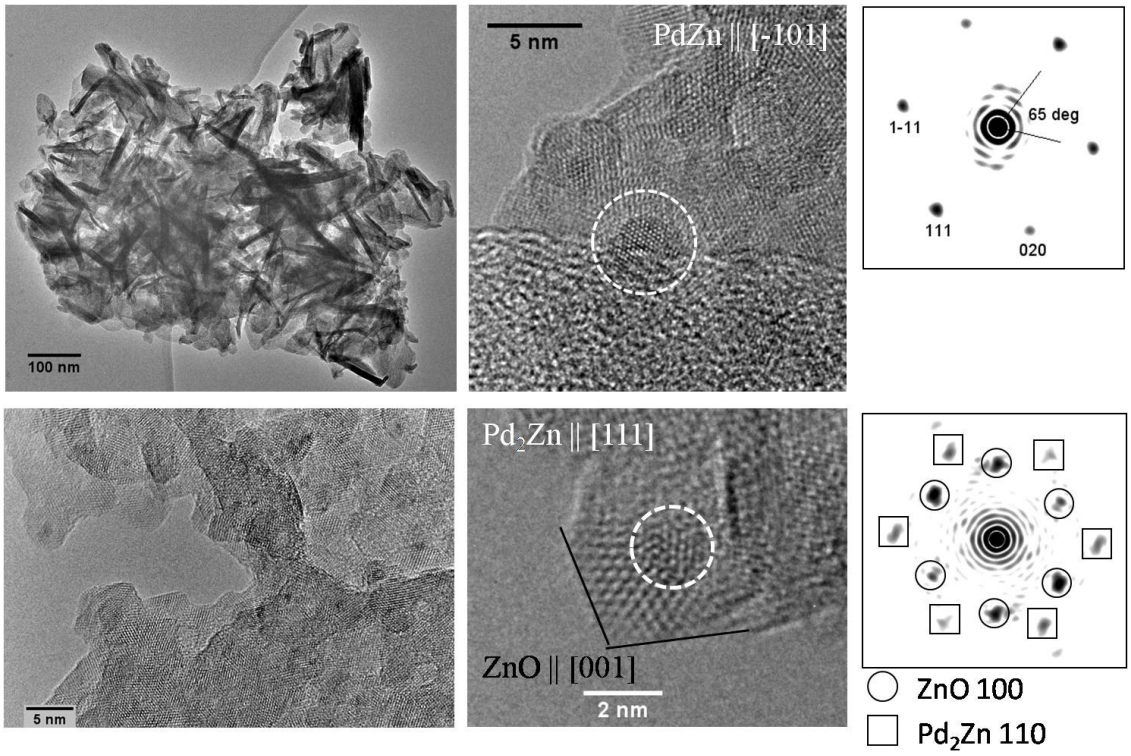

Figure 8: TEM images of PdZnAl after reduction at 250 °C in 5% H_2/Argon.

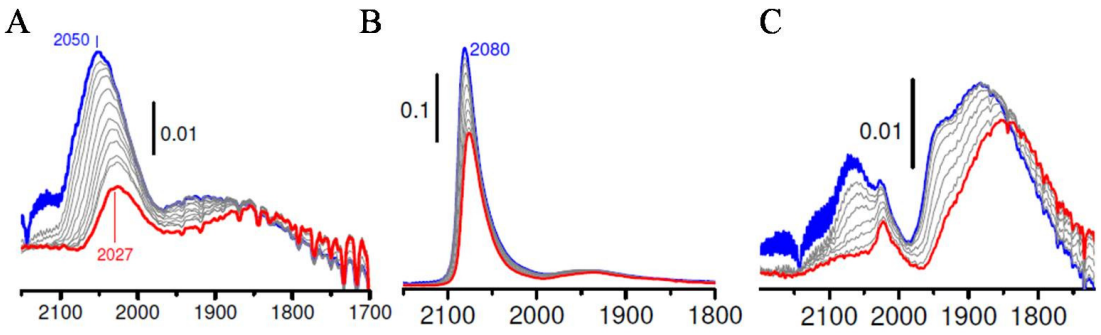

Figure 9: FT-IR spectra of CO adsorbed on (A) PdZnAl (reduced at 250 °C), (B) PdMgGa (reduced at 550 °C) and (C) PdMgAl (reduced at 250 °C) recorded at room temperature as a function of CO coverage (θ_{max}: blue, θ_{min}: red).

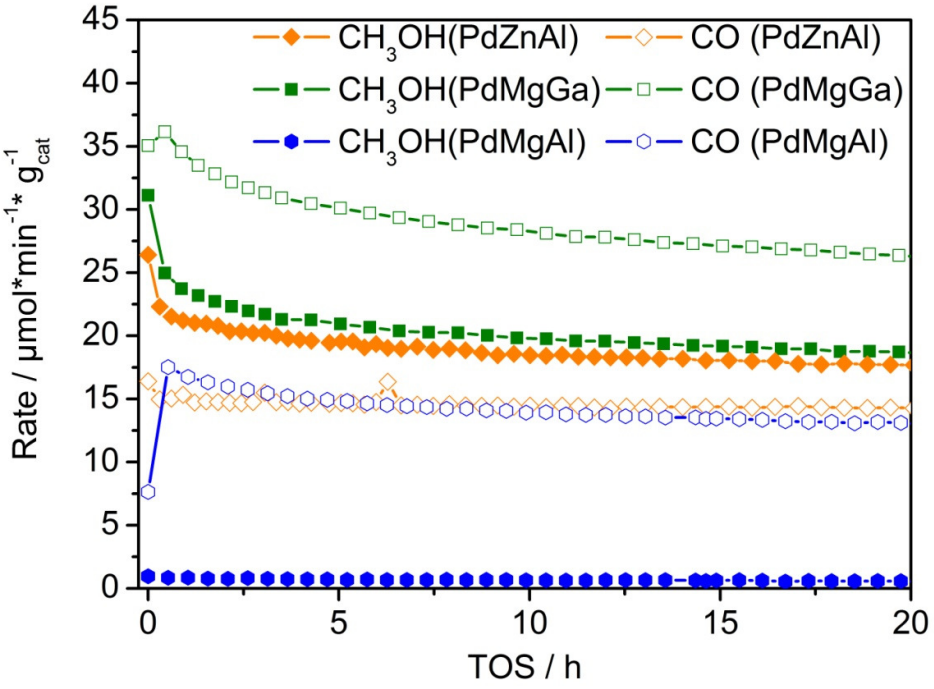

Figure 10: CO_2 hydrogenation over PdZnAl, PdMgGa and PdMgAl at 250 °C (30 bar, 400mg catalyst, 100 ml/min CO_2/H_2).

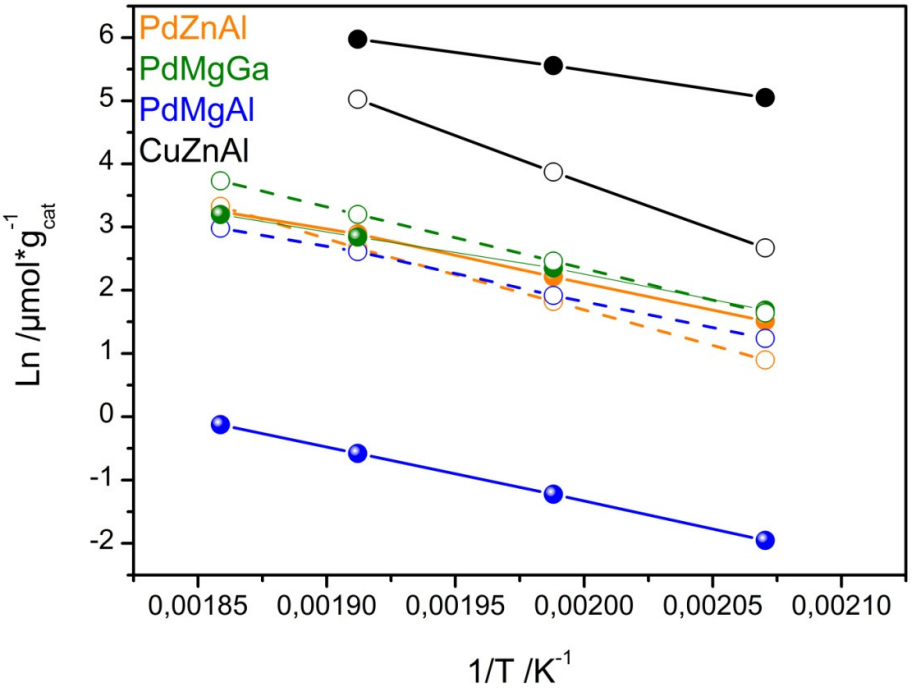

Figure 11: Arrhenius plot for methanol synthesis from CO_2 (closed symbols: MeOH, open symbol CO).

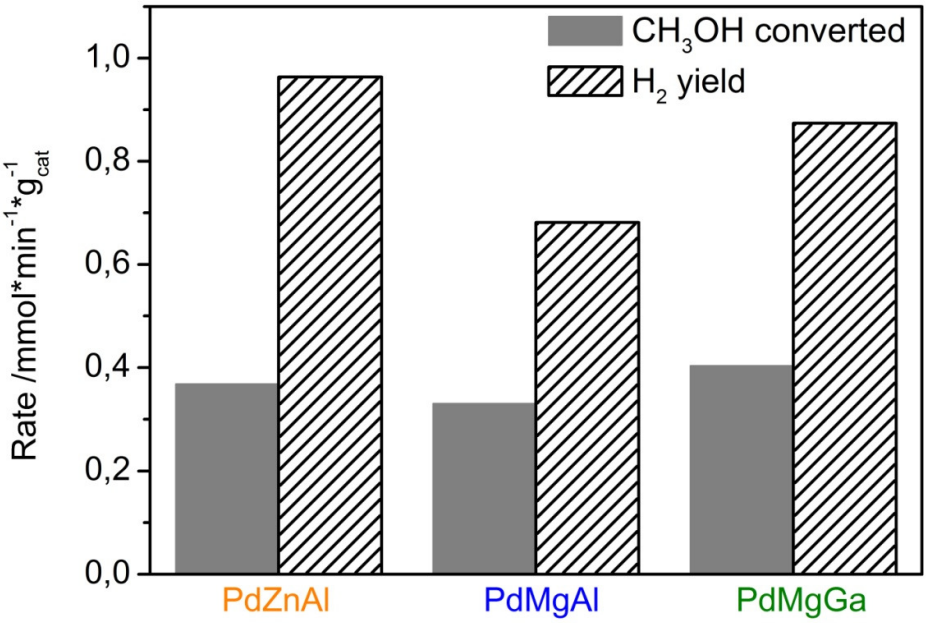

Figure 12: Reactivity results of PdZnAl, PdMgGa and PdMgAl catalysts in SRM conducted at 250 °C.

Table 1: Chemical composition and textural properties of the HTlc precursor materials.

Sample	Measured Composition[a] $Pd:M^{2+}:M^{3+}$	BET SA precursors [m^2/g]	BET SA reduced [m^2/g]	Pd content after reduction [wt%]	Particle size by TEM [nm]
ZnAl	0:70.3:29.7	53	n.d.[b]	-	-
PdZnAl	1.0:69.5:29.5	85	86[c]	1.46	1.8[c]
MgGa	0:63.2:36.8	34	130	-	-
PdMgGa	1.0:64.5:34.5	48	116[d]	1.81	6.1[d]
MgAl	0:65.6:34.4	111	n.d.[b]	-	-
PdMgAl	1.3:69.1:29.6	127	123[c]	3.13	2.2[d]

[a] determined by ICP-OES; [b] n.d. = not determined; [c] reduced at 250 °C; [d] reduced at 500 °C

Table 2: Activities for methanol synthesis from 1:3 CO_2:H_2 ratio at 30 bar on Pd-based and Cu-based catalysts at 250 °C.

Catalyst	**Metal site**[a] **[µmol/g_{cat}]**	**X_{CO2} [%]**	**Rate [µmol/min·g_{cat}]**		**Space velocity [mmol/g_{cat}-min]**	**S_{MeOH} [%]**	**TOF [min^{-1}]**	
			MeOH	**CO**			**MeOH**	**CO**
PdZnAl	73.4	0.6	9.1	6.2	10	60	0.12	0.08
PdMgGa	20.4	1.0	10.5	11.7	10	47	0.51	0.57
PdMgAl	90.9	0.3	0.3	6.8	10	4	0.003	0.07
CuZnAl	170.9[b]	5.0	67.3	47.6	10	59	0.39	0.28
		1.3	222.4	47.6	93	82	1.30	0.28

[a] estimated from the metal particle size determined by TEM, [b] measured with N_2O reactive frontal chromatography

Table 3: Activity results for the Pd-based IMC catalysts for the steam reforming of methanol at 250 ºC.

Catalyst	**Metal sites[a] [µmol/g)]**	**X_{MeOH} [%]**	**S_{CO2} [%]**	**Rate [µmol/min-g]**		**S_{H2} [%]**	**TOF [min^{-1}]**	
				Methanol converted	**H_2 released**		**MeOH**	**H_2**
PdZnAl	73	14.0	61.1	369	964	87	5.1	13.2
PdMgGa	20	15.3	16.4	404	874	72	20.2	43.7
PdMgAl	91	12.6	6.1	331	681	69	3.6	7.5

[a] estimated from the metal particle size determined by TEM

Supplementary Information

Sample identification

Label	FHI internal sample number
PdZnAl	11120
PdMgGa	10230
PdMgAl	9319
CuZnAl	9270

CuZnAl reference catalyst

The CuZnAl HTl precursor was precipitated from a $Cu^{2+}/Zn^{2+}/Al^{3+}$ nitrate solution (total metal concentration: 0.43M; Cu : Zn : Al = 50 : 17 : 33) with an aqueous solution of NaOH (0.3M) and Na_2CO_3 (0.045M) as the precipitating agent. The reaction was carried out at a constant pH value (pH = 8 ± 0.7) at 25 °C – pH and temperature were controlled by the automated lab reactor system (Labmax from Mettler Toledo). After an ageing time of one hour the blue powder was isolated by filtration, washing and drying at 100 °C for 13 h. Afterwards the sample was calcined in air at 330 °C for 3 h (heating rate 2°⁄min). The Cu based catalyst was obtained by in-situ reduction of the calcined sample in 5% H_2/Argon and a heating rate of 6 °⁄min at 330 °C for 30 min before the catalytic measurement was performed at 250 °C.

For the determination of the specific Cu surface area N_2O-reactive frontal chromatography (RFC) is used and carried out at 30 °C (Details see Ref. [20]). This technique is based on the decomposition of nitrous oxide molecules on the surface of copper to produce chemisorbed oxygen atoms and gas phase nitrogen. The Cu surface area was 7 m²/g.

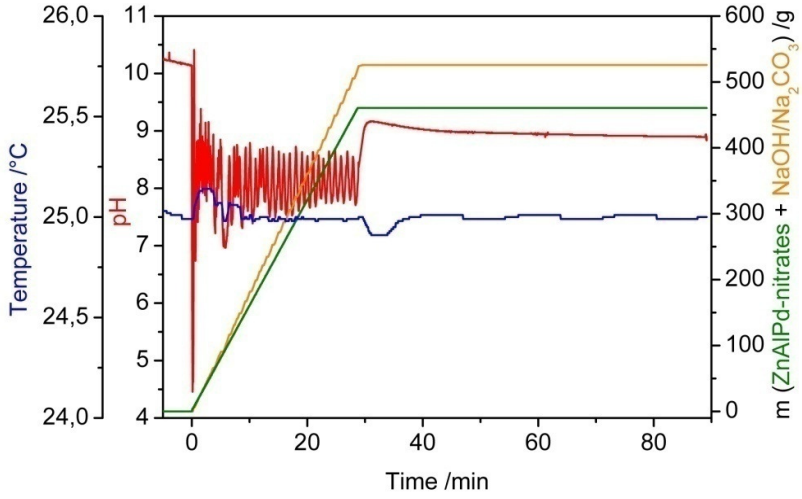
Temperature /°C
pH
m (ZnAlPd-nitrates + NaOH/Na2CO3) /g
Time /min

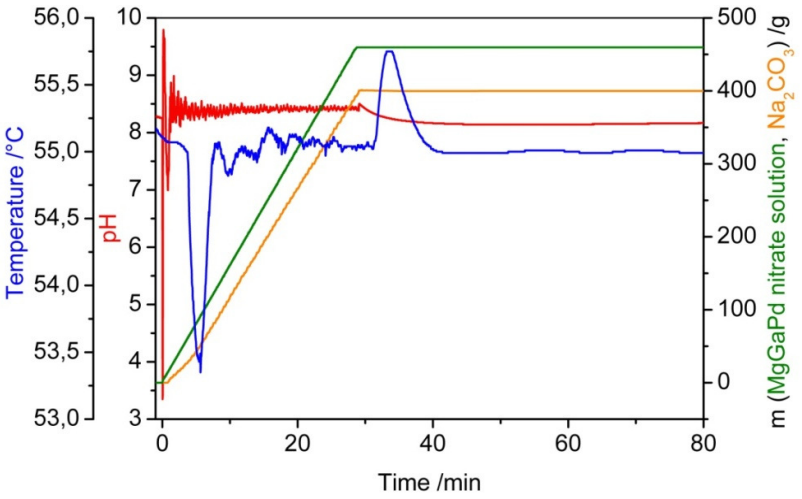
Temperature /°C
pH
m (MgGaPd nitrate solution, Na2CO3) /g
Time /min

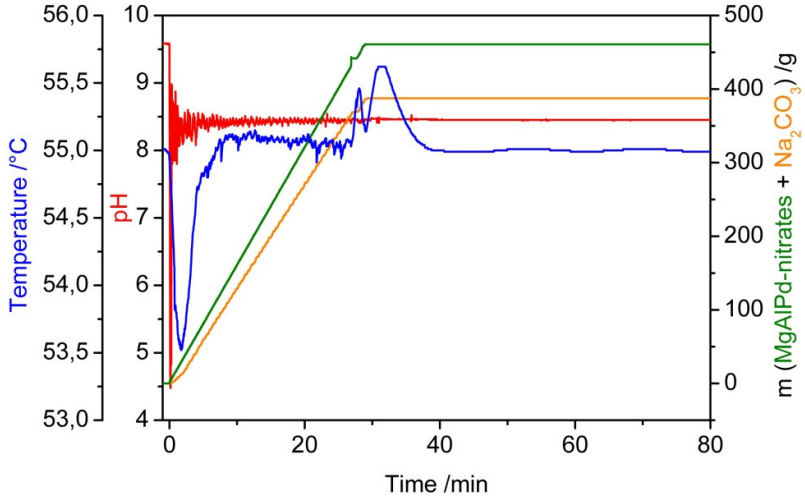

S 1: Synthesis protocol of PdZnAl, PdMgGa and PdMgAl precursors.

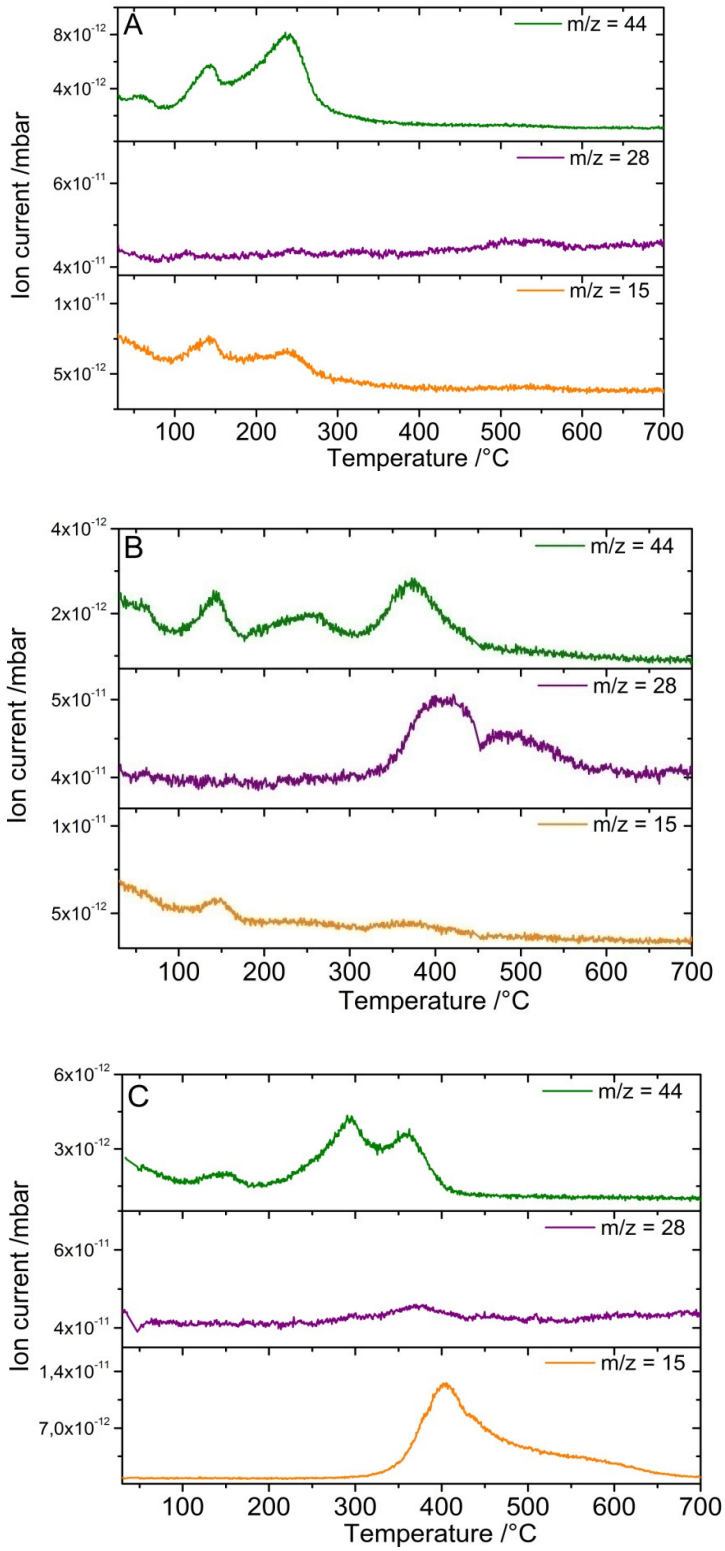

S 2: MS data of (A) PdZnAl, (B) PdMgGa and (C) PdMgAl HTlc precursor during heating in 5% H_2/Ar (2°C/min).

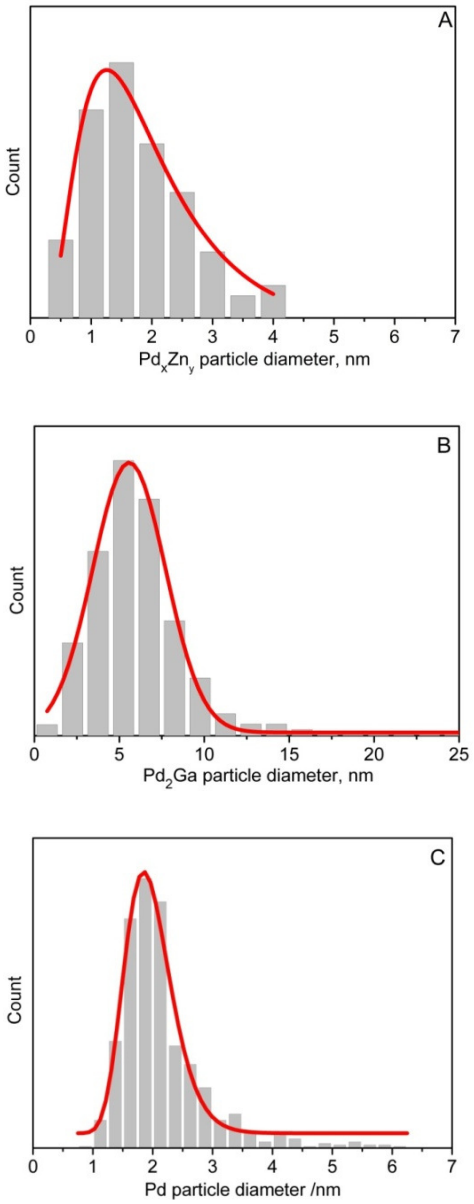

S 3: Particle size distribution of (A) PdZnAl reduced at 250 °C (B) PdMgGa reduced at 500 °C and (C) PdMgAl reduced at 250 °C.